Solar Physics
DOI: 10.1007/•••••-•••-•••-••••-•

Center–limb variation of solar photospheric microturbulence

Yoichi Takeda

Abstract Microturbulence (ξ) is a key parameter introduced in stellar spectroscopy to explain the strength of saturated lines by formally incorporating an additional thermal broadening term in the line opacity profile. Although our Sun can serve as an important testing bench to check the usual assumption of constant ξ, the detailed behavior of how ξ varies from the disk center through the limb seems to have never been investigated so far. In order to fill this gap, local ξ values on the solar disk were determined from the equivalent widths of 46 Fe I lines at 32 points from the center to the limb by requiring the consistency between the abundances derived from lines of various strengths. The run of ξ with θ (angle between line of sight and the surface normal) was found to be only gradual from ≈ 1.0 km s^{-1} (at $\sin\theta = 0$: disk center) to ≈ 1.3 km s^{-1} (at $\sin\theta \approx 0.7$: two-thirds of radial distance); but thereafter increasing more steeply up to ≈ 2 km s^{-1} (at $\sin\theta = 0.97$: limb). This result further suggests that the microturbulence derived from the flux spectrum of the disk-integrated Sun is by $\approx 20\%$ larger than that of the disk-center value, which is almost consistent with the prediction from 3D hydrodynamical model atmospheres.

Keywords: Center-Limb Observations; Spectral Line, Broadening; Spectrum, Visible; Turbulence; Velocity Fields, Photosphere

1. Introduction

It has been common in traditional stellar spectroscopy to invoke the very rough concept of micro/macro dichotomy in treating the effect of atmospheric turbulent velocity field on spectral lines: The "micro"-turbulence with its characteristic scale-length considerably smaller than the photon mean-free-path acts on the line *opacity* to broaden as in the case of the thermal motion of atoms, while conversely the "macro"-turbulence is a kind of global atmospheric motion which widens the emergent line *profile* similar to the case of rotational line broadening.

Especially, the former microturbulence (designated as ξ in this paper, which is incorporated in the thermal Doppler velocity term of line opacity profile as

11-2 Enomachi, Naka-ku, Hiroshima-shi 730-0851, Japan
email: ytakeda@js2.so-net.ne.jp

$\sqrt{2kT/m+\xi^2}$: k is Boltzmann constant, T is temperature, and m is atomic mass) plays a significant role in stellar chemical abundance determination as an indispensable fudge parameter, which especially affects the lines of moderately large strengths on the shoulder or flat part of the curve of growth. Since the effect of this parameter depends on line strengths, it is usually determined by requiring that the abundances derived from lines of diversified equivalent widths are consistent with each other, which means that measurement for a number of lines of the same species (*e.g.*, Fe I) is necessary.

Alternatively, another (rather special) method is applicable, which makes use of the fact that the core profile of saturated lines is critically influenced by ξ (*i.e.*, boxy shape becomes more manifest with an increase in ξ). In this case, Fourier transform technique is often employed, because such a subtle difference of line profile is more easily detected in the Fourier space (*e.g.*, position of zero amplitude frequency). Although ξ is in principle determinable from the profile of only one strong line, this approach is not so widely used in practice, since the results often show some inconsistencies with those from the conventional method.

Regarding the solar photospheric microturbulence, quite a few number of studies have been published so far, as shown in Table 1 which summarizes the data after 1976 (see also Table VI of Blackwell *et al.*, 1976, where older references in 1955–1972 are compiled). The following characteristics are read from these literature data of ξ for the Sun.

- Most of the results for solar ξ are around ≈ 1 km s^{-1} (within dispersion of $\approx \pm 0.5$km s^{-1}). As a matter of fact, $\xi = 1$ km s^{-1} is an often adopted assumption for the solar microturbulence (*cf.* Section 3.2 in Takeda, 1994).
- The microturbulence determined from line profile analysis appears somewhat lower than that derived by the conventional method requiring the consistency of abundances.
- The ξ values near to the limb tend to be larger than that those at the disk center.

The last point may be significant in context of conventional spectroscopic analysis of stars in general (unresolved point source) where a single-valued ξ has to be assumed. If microturbulence is variable over the disk, what kind of effect is expected on the result? As the only star whose surface is observable in detail, our Sun provides us with an opportunity to check this problem by clarifying the behavior of ξ from the disk center through the limb. Unfortunately, to the author's knowledge, this has never been seriously investigated so far. What has been reported is only the fact of variable ξ in a few sparse points at most (*e.g.*, Blackwell *et al.*, 1976; Holweger, Gehlsen, and Ruland, 1978; Gadun and Kostyk, 1990). This is presumably due to the necessity of equivalent widths measurements for a large number of lines to establish ξ, and repeating this process for many different points on the disk may have been felt reluctant.

Recently, Takeda and UeNo (2019; hereinafter refereed to as TU19) published the extensive equivalent width data set of 565 lines measured for 32 points (densely distributed from the solar disk center to the limb), which are just suitable for the task mentioned above. Motivated by this situation, the author

decided to investigate the nature of center–limb variation in ξ by making use of the data of TU19, and to examine how it affects the conventional procedure of using constant ξ in an application to disk-integrated spectrum. The aim of this article is to describe the outcome of this analysis.

2. Observational Data

Regarding the basic data of equivalent widths (W), those for 565 lines measured from the intensity spectra observed (by using the Domeless Solar Telescope at Hida Observatory of Kyoto University) at each of the 32 different positions on the solar disk were used, which were published by TU19 as supplementary materials (*cf.* Appendix A.3 therein).

Since the use of spectral lines with sufficiently reliable gf values is essential for the present purpose, the list of 65 Fe I lines adopted by Grevesse and Sauval (1999) for their solar Fe abundance analysis was invoked in this study. A comparison of these 65 lines with those 565 lines in TU19 revealed that 50 lines are in common. Then, after close inspection on these candidate lines, 4 lines turned out to show rather irregular and inadequate center–limb variation of W and were thus discarded. Consequently, 46 Fe I lines were decided to use as listed in Table 2, where the atomic parameters along with the equivalent widths at the disk center (W_{00}) and the limb (W_{31}) are also presented.[1] In order for a comparison purpose, flux equivalent widths for the disk-integrated Sun ($W_{\rm flux}$) were also measured for these 46 lines based on Kurucz *et al.*'s (1984) solar flux spectrum by applying the spectrum-fitting technique similar to that adopted in TU19 (*cf.* Section 3.1 therein; the only difference is that flux is relevant in this case instead of specific intensity).

Comparison of disk-center equivalent widths derived in TU19 (W_{00}) with those of Grevesse and Sauval (1999) ($W^{\rm GS}_{\rm d.c.}$) is shown in Figure 1a, which shows that the latter tends to be systematically larger than the former by $\approx 3\%$. Meanwhile, the $W_{\rm flux}$ values newly derived in this study are favorably compared with those of Takeda *et al.* (2005) (measured by the direct Gaussian fitting method), as displayed in Figure 1b.

Generally, Fe I lines tend to be strengthened with a decrease in temperature because of the negative sign of their T-sensitivity parameter (K_{00} given in Table 2), [2] which means that W increases toward the limb (*i.e.*, towards shallower line-forming layer with lowered T). Therefore, W_{31}/W_{00} is greater than unity and this tendency becomes more manifest towards a lesser K_{00} (*i.e.*, larger $|K_{00}|$) as can be seen in Figure 1c, where the natural inequality of $W_{00} < W_{\rm flux} < W_{31}$ is also confirmed.

[1] Complete data of W_{ii} ($ii = 00, \ldots, 31$) at 32 points between the center and the limb for these 46 lines are available in the supplementary material of TU19 ("all_clvdata").

[2] This parameter is indicative of the T-sensitivity of W_{00} at the disk center and defined as $K_{00} \equiv (d\log W/d\log T)_{00}$, which was numerically evaluated for each line (*cf.* Equation (6) in TU19).

Figure 1d shows the empirical curve of growth constructed from the disk center equivalent widths (W_{00}), which suggests that the adopted 46 Fe I lines are in the range of linear through flat part of the curve of growth.

3. Determination of Microturbulence

3.1. Procedures

As usually done, the value of ξ at each disk point was determined by requiring that the abundances derived from each of the 46 lines do not show any systematic dependence upon W. As in TU19, Kurucz's (1993) ATLAS9 model was adopted as the basic solar photospheric model, and likewise Kurucz's (1993) WIDTH9 program (though modified in various respects) was used for abundance calculation. Regarding the atomic parameters, Grevesse and Sauval's (1999) paper was consulted for $\chi_{\rm low}$ and $\log gf$ (*cf.* Table 2), while the adopted damping parameters are the same as given in "tableE.dat" of TU19.

Practically, the procedure employed by Blackwell *et al.* (1976) was followed in this investigation.

– 1. For each line n, a set of abundances ($\log \epsilon_n^m$; $m = 1, 2, \ldots, M$) were derived from W_n while incrementally changing the microturbulence (ξ^m; $m = 1, 2, \ldots, M$), where ξ was varied from 0.0 to 2.6 km s^{-1} by an increment of 0.01 km s^{-1} (*i.e.*, $M = 261$).

– 2. Then, the mean abundance ($\langle \log \epsilon \rangle^m$) averaged over $N(= 46)$ lines and the standard deviation σ^m were derived for each of the M microturbulences (ξ^m).

– 3. By inspecting the resulting set of (σ^m, $m = 1, 2, \ldots, M$), the location of minimum σ corresponds to desired solution, which is denoted by the subscript "0" such as ξ_0 (and likewise σ_0 or $\langle \log \epsilon \rangle_0$.

Such as done by Blackwell *et al.* (1976) in their Figs. 1 and 2, the $\log \epsilon$ *vs.* ξ relations for each of the 46 lines along with the resulting σ *vs.* ξ curve are illustrated in Figure 2 for the representative 6 points on the disk (panels a–f), where the results for the disk center based on Grevesse and Sauval's (1999) $W_{\rm d.c.}$ (panel g) as well as for the disk-integrated Sun based on $W_{\rm flux}$ (panel h) are also presented.

3.2. Error estimation

While the mean error of $\langle \log \epsilon \rangle_0$ is naturally expressed as $\sigma_0/\sqrt{N}$, it is not straightforward to estimate how much error is involved in ξ_0. In this study, it was derived as follows.

– Since the abundance for each line has an uncertainty of σ, randomly-generated noises (Δ) of normal distribution (corresponding to a dispersion of σ_0) were added to the set of actual abundances as ($\log \epsilon_n + \Delta_n$, $n = 1, 2, \ldots, N$), from which a new standard deviation (σ') was computed and this process was repeated 1000 times ($k = 1, 2, \ldots, 1000$).

– Next, the standard deviation evaluated on a data set of ($\sigma'_k/\sqrt{2}$, $k = 1, 2, \ldots, 1000$)

was denoted as $\delta\sigma$,[3] which may be regarded as the ambiguity in the $\sigma(\xi)$ curve around the minimum.
– Finally, the error ($\delta\xi$) involved in ξ_0 was estimated from the intersection points of the $\sigma(\xi)$ curve and the $\sigma = \sigma_0 + \delta\sigma$ line, as they correspond to $\xi_0 \pm \delta\xi$ (see Figure 2i, where this situation is graphically depicted). The resulting $\delta\xi$ turned out typically on the order of ≈ 0.2 km s^{-1}.

4. Discussion

4.1. Resulting trends

The finally established values of $\langle \log \epsilon \rangle_0$, σ_0, ξ_0, and $\delta\xi$ at each of the 32 points on the disk are given in Table 3, where the results derived from $W^{\rm GS}_{\rm d.c.}$ as well as $W_{\rm flux}$ are also presented for comparison. In addition, the runs of these quantities from the disk center to the limb are graphically illustrated in Figure 3. The following characteristics are read from these results.

- The $\langle \log \epsilon \rangle_0$ values at different disk points are remarkably similar (mean over the 32 points is 7.411 with a standard deviation of 0.005). Likewise, the σ_0 values do not vary significantly from the center (≈ 0.07) to the limb (≈ 0.08). This implies that the classical line formation theory using the microturbulence is practically validated irrespective of observed points on the disk (as far as abundance determination is concerned).
- While a systematically increasing trend is surely observed in ξ_0 towards the limb, its rate is position-dependent in the sense that a steeper gradient is seen near to the limb. Actually, the growth of ξ_0 is only gradual at first from ≈ 1.0 km s^{-1} (disk center) to ≈ 1.3 km s^{-1} (at $\sin\theta \approx 0.7$: two-thirds of the radial distance); but it begins thereafter to increase more steeply until reaching ≈ 2 km s^{-1} at the limb ($\sin\theta = 0.97$).

Some previous authors have determined ξ values at different points on the solar disk (*e.g.*, Blackwell *et al.*, 1976; Holweger, Gehlsen, and Ruland, 1978; Gadun and Kostyk, 1990) as summarized in Table 1. Since the observations of these literature studies were restricted to only a few points (usually at the disk center and the limb), they are too coarse to be compared with the ξ *vs.* θ trend derived in this investigation, Nevertheless, our ξ values are more or less consistent with these results (within error bars) showing the same tendency of ξ(center) $<$ ξ(limb).

4.2. Reference formula for ξ

It is useful to derive an analytical expression for the θ-dependent ξ as a reference model in preparation for the test calculations presented in the following sections.

[3]Note that σ' should be divided by $\sqrt{2}$ in order to avoid duplication, because the original abundance set already has an intrinsic dispersion of σ_0,

For this purpose, a slight pre-adjustment was applied to the original data of ξ_0 *vs.* θ relation. Although its disk-center value is 1.13 km s^{-1}, the standard value of 1.0 km s^{-1} had better be adopted in order to maintain consistency with TU19, where this value was used in deriving K_{00} or $\log \epsilon_{00}$. Therefore, $\xi_0(\theta)$ was divided by 1.13 to obtain the normalized $\xi_{\rm n}(\theta)$ to be employed, which is a practically valid procedure given that ξ_0 is already uncertain by $\pm$0.2 km s^{-1} (at any rate, our main concern is not so much the absolute values as the relative variation of ξ on the disk).

The resulting $\xi_{\rm n}(\theta)$ values are presented in the 8th column of Table 3. By applying a least-squares fitting with second-order polynomials (in terms of $\cos\theta$) to these data, the following analytical expression was found to yield a satisfactory fit

$$\xi_{\rm n}({\rm km\ s^{-1}}) = 1 + 0.0649(1-\cos\theta) + 1.427(1-\cos\theta)^2 \qquad (1)$$

as demonstrated in Figures 4a and 4b.

It is worth mentioning that the $\xi_{\rm n}$ *vs.* θ relation expressed in terms of $\cos\theta$ shows a rather monotonically increasing trend towards the limb (Figure 4a), whereas the rate of increase becomes appreciably steeper near to the limb if $\sin\theta$ is used (Figure 4b). This difference stems from the fact that, while specifying the disk position by $\sin\theta$ is in accord with the apparent view of the solar disk, the scale is more expanded near to the limb in case of using $\cos\theta$.

4.3. Consistency check

It is worthwhile to confirm the validity of such obtained reference $\xi_{\rm n}(\theta)$ relation by checking that it does not cause any inconsistency with other available information.

The first test is to find a empirical $\xi(\theta)$ relation by demanding that the abundances derived from $W(\theta)$ do not depend upon θ. In this method, the run of ξ with θ can be evaluated from any single spectral line of sufficient strength, though ξ at some fiducial point (*e.g.*, disk center) should be given in advance. That is, the disk center abundance $\log \epsilon_{00}$ was first derived from W_{00} by assuming $\xi = 1$ km s^{-1}; and the values of ξ for the remaining points ($ii = 01, 02, \ldots, 31$) were determined from W_{ii} by requiring that the abundance ($\log \epsilon_{ii}$) be equal to $\log \epsilon_{00}$. This procedure was applied to 15 lines (selected out of 46 lines) of medium-to-large strengths ($W_{00} \geq 50$ mÅ) and the resulting $\xi(\theta)$ relations are overplotted in Figures 4c and 4d, where the curve expressed by Equation (1) is also depicted for comparison. We can see from these figures that the resulting trends (at least in the relative sense) are in reasonable agreement with each other.

The second check is to revisit the task once addressed in Appendix 1 of Takeda (2019), who examined the mutual consistency of solar Fe abundances derived at various points on the disk by adopting a constant microturbulence of $\xi = 1$ km s^{-1}. In Figures 10a–10d of that paper, the abundance differences relative to the disk-center value are plotted against $\cos\theta$, which were derived for 280 Fe I lines (divided into 4 groups according to the line strengths) based on W values published by TU19. Those figures evidently indicated the existence of

systematic discrepancies increasing toward the limb. Then, what would happen if θ-dependent ξ given by Equation (1) is used instead of $\xi = 1$ km s^{-1}? The answers are shown in Figures 5a–5d, which are arranged in the same manner as the case of Takeda's (2019) Figures 10a–10d for the sake of enabling a direct comparison. These figures suggest that the use of $\xi(\theta)$ has considerably removed the serious inconsistencies (seen in the case of constant ξ) to a satisfactory level, which may be counted as another evidence for the validity of the result in this study.[4]

4.4. Impact on flux spectrum analysis

Now that how the microturbulence varies over the solar disk has been established, it is interesting to examine how such a position-dependent ξ affects the spectrum analysis of the Sun-as-a-star where a constant ξ is usually assumed. For this purpose, the theoretical profiles (and the corresponding equivalent widths) of spectral lines were simulated by using θ-dependent ξ, which were further analyzed inversely in the conventional manner by assuming a constant microturbulence. See Section 3.5 in Takeda (2019) for the adopted program code of line profile simulation.

First, the examination was done on the usual microturbulence determination method. After the $W_{\rm cal,flux}$ values (theoretical equivalent width for the disk-integrated Sun) were calculated for 46 Fe I lines by assuming $\log\epsilon = 7.43$ and $\xi_{\rm n}(\theta)$ (Equation (1)), the critical ξ^* value was derived for each line that yields an abundance of 7.43 by the classical analysis on $W_{\rm cal,flux}$. The ξ^* *vs.* $W_{\rm cal,flux}$ relations are depicted in Figure 6a, where the plots are limited to lines of $W_{\rm cal,flux} > 10$ mÅ because too weak lines are insensitive to ξ. Besides, the abundances ($\log\epsilon$) were derived from $W_{\rm cal,flux}$ values of 46 lines for three cases of microturbulence (1.1, 1.2, and 1.3 km s^{-1}). The resulting $\log\epsilon$ *vs.* $W_{\rm cal,flux}$ plots are shown in Figure 6b. These figures suggest that a conventional ξ-determination based on the $W_{\rm cal,flux}$ data leads to a result of $\xi \approx 1.2$ km s^{-1}.

Next, the influence on ξ-determination from the profile of a saturated line was investigated, which is often done by the location of first zero in the Fourier transform of line profiles. Here, the high-quality Fe I line at 6252.554 Å ($W_\odot \approx$ 124 mÅ; occasionally used for this purpose; *e.g.*, Gray, 1977) was adopted as the representative test line. After the line depth profiles, $D(\lambda) \equiv 1 - F_\lambda/F_{\rm cont}$, were simulated for 6 cases of different conditions (*cf.* Table 4), their Fourier transforms, $d(\sigma) \equiv \int D(\lambda)\exp(2\pi i\lambda){\rm d}\lambda$, were computed as illustrated in Figure 7.[5]

[4]In Takeda (2019), an analytical formula of $\xi = 1 + 0.6\sin\theta$ (km s^{-1}) was applied as the θ-dependent solar microturbulence, which was tentatively devised in analogy with the θ-dependence of the macroturbulence. That relation was not appropriate as viewed from the present knowledge, since it does not correctly reproduce the characteristic trend in terms of the increasing rate of ξ (becoming steeper towards the limb).

[5]Meaningful information can also be read from Figure 7c, First, q_1 is only marginally influenced (*i.e.*, slightly shifting to higher frequencies) by inclusion of macroturbulence and rotation as seen from the results of Cases 1–3. Second, the first zero of the rotational broadening function (so-called Carroll's zero) is not observed at all in the transform for Case 3, which means that the rotational effect on the profile is no more expressed by a convolution of the broadening function for the case of slow rotators (*cf.* Takeda, 2019).

Since the positions of the first zero (q_1) are 0.143–0.148 km^{-1}s when the realistic θ-dependent ξ is used (Cases 1, 2, and 3), this corresponds to $\xi \approx$1.1–1.2 km s^{-1} in the conventional assumption of constant ξ, as expected from the q_1 values for Cases 0a, 0b, and 0c (0.170, 0.150, and 0.133 km^{-1}s; *cf.* Table 4).[6]

Both of the two tests described above have suggested that ξ values resulting from the solar disk-integrated spectrum tend to be slightly larger by $\sim 20\%$ than that at the disk center. This is a natural consequence in a sense, because the flux spectrum may be regarded as roughly equivalent to the intensity spectrum at $\mu = \cos\theta = 2/3$ (so-called Eddington–Barbier relation), where Equation (1) yields $\xi = 1.18$ km s^{-1}. Alternatively, the mean $\langle\xi\rangle$ averaged over the solar disk may be expressed as

$$\langle\xi\rangle = \int_0^{\pi/2} I(\theta)\xi(\theta)\sin\theta\cos\theta \mathrm{d}\theta \Big/ \int_0^{\pi/2} I(\theta)\sin\theta\cos\theta \mathrm{d}\theta. \tag{2}$$

Let us further write the θ-dependence of the continuum specific intensity as

$$I(\theta) = I_0(1 - u + u\cos\theta), \tag{3}$$

where I_0 is the disk center intensity and u is the limb-darkening coefficient (around ≈ 0.7 for the case of the Sun at the visual region of $\lambda \approx$ 5000–6000 Å; *cf.* Fig. 17.6 in Gray, 2005). Inserting Equations (1) and (3) to Equation (2), we obtain $\langle\xi\rangle = 1.20$ km s^{-1}. Accordingly, ξ(flux) is expected to be slightly larger than ξ(center) by $\approx 20\%$ from Equation (1). Although this inequality is not clearly confirmed in our results in Table 3, such a tendency is observed in the literature data in Table 1.

4.5. Physical cause of center–limb variation

Finally, it is worth briefly mentioning the physical background regarding the systematic increase of ξ towards the limb. Historically, this trend was occasionally discussed (especially until 1970s) in terms of its height-dependence or intrinsic anisotropy. However, such a classical interpretation appears to be of limited significance, because microturbulence itself is not so much a physically well-defined entity as a practically useful fudge parameter.

In any case, the former explanation is unlikely, because ξ is reported to rather decrease with height in the solar photosphere (*e.g.*, Gray, 1978) from 1 km s^{-1} ($\tau_{5000} \approx 1$) to 0.5 km s^{-1} ($\tau_{5000} \approx 10^{-3}$); thus, ξ would rather decrease toward the limb (contrary to the observational fact) as the line-forming layer moves progressively higher. Likewise, the latter anisotropic microturbulence model does not seem to be relevant. If a simple anisotropic Gaussian microturbulence model is assumed, the θ-dependence of ξ would be described as $\xi(\theta)^2 = (\xi_\mathrm{R}\cos\theta)^2 +$

[6]It should not be misunderstood that $\xi \approx$1.1–1.2 km s^{-1} is actually derived for the Sun from the line flux profile analysis. As briefly remarked in Section 1, ξ(profile) tends to be lower than ξ(EW); for example, Gray (1977) derived $\xi = 0.5$ km s^{-1} from the profile analysis of Fe I 6252.554 line. See, *e.g.*, Section 4.3 in Takeda *et al.* (1996) for a consideration on this discrepancy.

$(\xi_{\rm T}\sin\theta)^2$, where $\xi_{\rm R}$ and $\xi_{\rm T}$ are the radial and tangential components. which may be set as 1 km s^{-1} and 2 km s^{-1} in the present case, respectively. The ξ *vs.* θ relation expected in this case is shown in Figures 4a and 4b (dashed line) for comparison, where we can see that this does not fit the observed trend at all.

The reason why more or less saturated lines show strength excess towards the limb (eventually causing an apparent increase in ξ) should be attributed to a more intricate process in which inhomogeneous velocity fields are involved in a complex manner. For example, Nordlund (1980) showed based on his 3D hydrodynamical calculations that, while the line intensification near the disk center is caused by the velocity gradients associated with time-dependent granular motions, the strengthening near to the limb is attributed rather to a geometrical effect due to the existence of velocity fluctuations along the line of sight penetrating more granular cells. Accordingly, it is requisite to invoke 3D hydrodynamical model atmospheres for understanding the nature of center–limb variations in ξ. In this context, Steffen, Caffau, and Ludwig's (2013) theoretical investigation on the apparent behaviors of classical micro/macro-turbulence based on CO5BOLD 3D model atmospheres is worthwhile to mention. Although the detailed center–limb trends of these parameters are not presented, their simulations indicate ξ(flux)/ξ(center) ratios of $\approx$ 1.2–1.3, when the results at the same attributes (species, equivalent widths, excitation potential, *etc.*) are compared with each other (*cf.* their Figures 1 and 3). This extent of theoretical ratio predicted from 3D calculations is almost consistent with the empirical results (around $\approx$ 1.2) discussed in Section 4.4, which is satisfying.

5. Summary and Conclusion

Microturbulence (ξ) is an important parameter in stellar spectroscopy, which was originally introduced by the necessity of reproducing the enhanced strength of saturated lines. Formally, this parameter is included (as if an additional thermal broadening) in the Doppler broadening of line opacity profile, while implicitly assuming that the characteristic scale-length of the relevant turbulent velocity field is considerably smaller than the photon mean-free-path.

Although it has been suggested that this ξ at the limb tends to be larger than that at the disk center, the detailed behavior regarding how ξ changes on the solar disk has not been investigated so far. The purpose of this study was to clarify this point.

As such, the ξ values were determined from the equivalent widths of 46 Fe I lines measured on the 32 points from the center to the limb, by following the conventional requirement that the abundances derived from different lines do not show any systematic dependence upon the line strengths, where Blackwell *et al.*'s (1976) procedure (searching for minimum abundance dispersion) was adopted in practice. At each point, the solution of ξ could be successfully established, and the mean Fe abundance $\langle\log\epsilon\rangle$ was also derived as a by-product.

The resulting $\langle\log\epsilon\rangle$ values turned out remarkably constant irrespective of the position on the solar disk (the mean averaged over 32 points is 7.411 with a standard deviation of 0.005), which may suggest that the classical line formation

treatment is practically valid at any point regardless of θ (as long as abundance determination is concerned).

The systematic trend of increasing ξ towards the limb could be confirmed. More precisely, the run of ξ (with a probable error of $\approx \pm 0.2$ km s^{-1}) with θ is only gradual from ≈ 1.0 km s^{-1} (at $\sin\theta = 0$: disk center) to ≈ 1.3 km s^{-1} (at $\sin\theta \approx 0.7$: two-thirds of radial distance), while increasing thereafter more steeply up to ≈ 2 km s^{-1} (at $\sin\theta = 0.97$: limb).

Based on the derived ξ *vs.* θ relation, test calculations were performed to see how much microturbulence (if assumed constant) would be obtained from the flux spectrum of the disk-integrated Sun. It revealed that ξ(flux) is about $\approx 20\%$ larger than than ξ(center). This result is consistent with the prediction from 3D hydrodynamical calculations carried out by Steffen, Caffau, and Ludwig (2013).

Disclosure of Potential Conflicts of Interest

The author declares that he has no conflicts of interest.

References

Blackwell, D.E., Ibbetson, P.A., Petford, A.D., Willis, R.B.: 1976, *Mon. Not. Roy. Astron. Soc.* **177**, 227. DOI: 10.1093/mnras/177.1.227

Blackwell, D.E., Booth, A.J., Petford, A.D.: 1984, *Astron. Astrophys.* **132**, 236.

Gadun, A.S., Kostyk, R.I.: 1990, *Sov. Astron.* **34**, 260.

Gadun, A.S.: 1994, *Astron. Nachr.* **315**, 413. DOI: 10.1002/asna.2103150604

Gray, D.F.: 1977, *Astrophys. J.* **218**, 530. DOI: 10.1086/155706

Gray, D.F.: 1978, *Solar Phys.* **59**, 193. DOI: 10.1007/BF00951830

Gray, D.F.: 2005, *The Observation and Analysis of Stellar Photospheres*, 3rd ed. (Cambridge University Press, Cambridge).

Grevesse, N., Sauval, A.J.: 1999, *Astron. Astrophys.* **347**, 348.

Holweger, H., Gehlsen, M., Ruland, F.: 1978, *Astron. Astrophys.* **70**, 537.

Kurucz, R.L.: 1993, *Kurucz CD-ROM No. 13*, Harvard-Smithsonian Center for Astrophysics, Cambridge, MA.

Kurucz, R.L., Furenlid, I., Brault, J., Testerman, L.: 1984, in *Solar Flux Atlas from 296 to 1300 nm*, Sunspot, New Mexico, National Solar Observatory.

Meylan, T., Furenlid, I., Wiggs, M.S., Kurucz, R.l.: 1993, *Astrophys. J. Suppl.* **85**, 163. DOI: 10.1086/191759

Nordlund, A.: 1980, in *Stellar Turbulence, IAU Colloq. 51*, ed. D. F. Gray, and J. L. Linsky (Springer, Berlin), p. 213. DOI: 10.1007/3-540-09737-6_33

Pavlenko, Ya.V., Jenkins, J.S., Jones, H.R.A., Ivanyuk, O., Pinfield, D.J.: 2012, *Mon. Not. Roy. Astron. Soc.* **422**, 542. DOI: 10.1111/j.1365-2966.2012.20629.x

Sheminova, V.A.: 2017, *Kinematika Fiz. Nebesnykh. Tel* **33**, 27. DOI: 10.15407/kfnt2017.05.027

Sheminova, V.A.: 2019, *Kin. Phys. Cel. Bodies* **35**, 129. DOI: 10.3103/S088459131903005X

Sheminova, V.A., Gadun, A.S.: 1998, *Kinematika Fiz. Nebesnykh. Tel* **14**, 219.

Steffen, M., Caffau, E., Ludwig, H.-G,: 2013, *Mem. S. A. It. Suppl.* **24**, 37.

Takeda, Y.: 1994, *Publ. Astron. Soc. Japan* **46**, 53.

Takeda, Y.: 1995, *Publ. Astron. Soc. Japan* **47**, 337.

Takeda, Y.: 2019, *Publ. Astron. Soc. Japan* **72**, 10. DOI:10.1093/pasj/psz129

Takeda, Y., Kato, K., Watanabe, Y., Sadakane, K.: 1996, *Publ. Astron. Soc. Japan* **48**, 511. DOI: 10.1093/pasj/48.3.511

Takeda, Y., Ohkubo, M., Sadakane, K.: 2002, *Publ. Astron. Soc. Japan* **54**, 451. DOI:10.1093/pasj/54.3.451

Takeda, Y., Ohkubo, M., Sato, B., Kambe, E., Sadakane, K.: 2005, *Publ. Astron. Soc. Japan* **57**, 27. DOI: 10.1093/pasj/57.1.27

Takeda, Y., UeNo, S.: 2019, *Solar Phys.* **294**, 63 (TU19). DOI:10.1007/s11207-019-1455-1

Table 1. Literature data of solar microturbulence (after 1976).

Reference (1)	Obs.part (2)	μ (3)	ξ (4)	Method (5)	Remark (6)
Blackwell *et al.* (1976)	center	1.0	0.80	EW	
	outer disk	0.5	1.25	EW	
	limb	0.3	1.40	EW	
	limb	0.2	1.70	EW	
	flux	—	1.18	EW	
Gray (1977)	flux	—	0.5	profile	
Holweger, Gehlsen, and Ruland (1978)	center	1.0	1.0	EW	
	limb	0.3	1.6	EW	
Blackwell, Booth, and Petford (1984)	center	1.0	0.85	EW	
Gadun and Kostyk (1990)	center	1.0	0.89	EW	mean of 6 values in Table I therein
	limb	0.2	1.84	EW	mean of 5 values in Table I therein
	flux	—	1.07	EW	mean of 4 values in Table I therein
Gadun (1994)	center	1.0	0.81	EW	result from Fe I lines
	flux	—	1.11	EW	result from Fe I lines
	center	1.0	0.86	EW	result from Fe II lines
	flux	—	1.20	EW	result from Fe II lines
Takeda (1995)	flux	—	0.51	profile	mean of 15 lines with Case-C solutions
Sheminova and Gadun (1998)	flux	—	0.8	profile	
Grevesse and Sauval (1999)	center	1.0	0.8	EW	
Takeda, Ohkubo, and Sadakane (2002)	center	1.0	0.76	EW	use of Grevesse and Sauval's (1999) EW
	flux	—	0.79	EW	use of Meylan *et al.*'s (1993) EW
	flux	—	0.86	EW	use of EW measured by themselves
Takeda *et al.* (2005)	flux	—	0.96	EW	Moon spectrum
Pavlenko *et al.* (2012)	flux	—	0.75	EW	result from Fe I lines
	flux	—	1.5	EW	result from Fe II lines
Sheminova (2017)	flux	—	0.85	profile	
Sheminova (2019)	flux	—	0.78	profile	

(1) References. (2) Observed part of the Sun (where "flux" means the disk-integrated spectrum of Sun-as-a-star). (3) Value of direction cosine μ ($\equiv \cos\theta$) at the point of observation. (4) Method of determination, where "EW" is the standard method using the equivalent widths of spectral lines, while "profile" is based on the analysis of spectral line profiles (mostly by using the Fourier technique, except for the usual profile fitting method adopted by Takeda, 1995). (5) Resulting value of microturbulence (in km s^{-1}). (6) Specific remarks.

Table 2. Atomic and observational data of adopted 46 Fe I lines.

λ (1)	$\chi_{\rm low}$ (2)	$\log gf$ (3)	$W^{\rm GS}_{\rm d.c.}$ (4)	W_{00} (5)	W_{31} (6)	$W_{\rm flux}$ (7)	K_{00} (8)
5225.533	0.110	−4.789	70.3	66.9	89.2	70.1	−4.97
5247.059	0.087	−4.946	65.6	62.4	81.0	65.2	−5.52
5250.217	0.121	−4.938	65.5	61.1	84.0	64.0	−5.69
5326.145	3.570	−2.071	34.5	30.5	37.7	33.0	−5.77
5412.788	4.440	−1.716	19.1	18.6	24.9	20.7	−5.59
5600.227	4.260	−1.420	36.5	27.6	32.5	29.6	−5.24
5661.348	4.280	−1.756	22.0	19.2	25.1	21.0	−5.86
5696.093	4.550	−1.720	13.4	9.1	11.5	12.4	−6.00
5701.553	2.560	−2.216	86.0	80.9	92.1	82.6	−3.11
5705.468	4.300	−1.355	39.7	34.9	39.8	36.9	−4.64
5778.458	2.590	−3.440	20.2	15.6	24.8	19.0	−9.20
5784.661	3.400	−2.530	25.4	22.1	30.1	24.9	−7.14
5855.080	4.610	−1.478	21.7	18.6	25.4	21.2	−5.28
5909.978	3.210	−2.587	30.0	23.4	29.5	24.8	−7.27
5956.700	0.859	−4.605	50.3	47.7	65.1	51.1	−7.51
6082.715	2.223	−3.573	33.8	27.5	42.4	33.7	−8.47
6120.255	0.910	−5.970	4.8	2.9	6.1	4.5	−14.69
6151.622	2.176	−3.299	48.5	43.1	60.3	49.0	−6.57
6180.208	2.730	−2.586	56.0	47.1	59.8	50.0	−5.47
6200.320	2.609	−2.437	75.4	70.1	84.1	70.9	−3.67
6219.289	2.198	−2.433	91.0	85.0	103.9	85.8	−3.40
6232.649	3.650	−1.223	88.4	82.7	92.9	81.8	−3.01
6240.652	2.220	−3.233	47.6	44.5	58.6	47.2	−6.36
6265.141	2.176	−2.550	86.7	84.8	99.5	83.6	−3.48
6271.283	3.330	−2.703	20.5	19.8	27.2	21.5	−7.55
6297.801	2.223	−2.740	74.8	71.8	85.6	71.3	−3.91
6311.505	2.830	−3.141	27.0	20.8	29.7	25.8	−8.30
6322.694	2.588	−2.426	79.2	68.4	79.1	73.0	−3.80
6353.840	0.910	−6.477	1.4	0.9	1.6	1.3	−15.21
6481.878	2.279	−2.984	64.2	57.6	65.7	60.6	−4.97
6498.946	0.958	−4.699	43.7	40.8	56.3	44.3	−8.68
6518.374	2.830	−2.450	57.0	50.6	58.3	52.5	−5.15
6574.233	0.990	−5.004	25.7	22.8	37.7	27.5	−11.51
6581.214	1.480	−4.680	17.0	13.7	22.2	16.3	−11.64
6593.880	2.433	−2.422	86.5	81.7	91.0	81.6	−3.47
6609.119	2.559	−2.692	65.3	60.5	67.5	61.3	−4.50
6625.027	1.010	−5.336	13.5	11.6	20.7	14.6	−12.74
6667.721	4.580	−2.112	8.9	8.0	9.8	8.8	−6.10
6699.142	4.590	−2.101	8.0	6.6	8.6	7.7	−6.13
6750.160	2.424	−2.621	76.2	71.4	81.0	72.8	−3.85
6752.711	4.640	−1.204	37.3	32.4	35.8	34.2	−4.46
6793.266	4.080	−2.326	12.6	10.3	13.8	12.0	−6.98
6804.003	4.650	−1.496	21.4	16.2	17.5	18.0	−5.51
6804.277	4.580	−1.813	14.9	11.6	13.5	13.5	−5.98
6837.009	4.590	−1.687	17.7	15.1	17.5	16.3	−5.74
6854.828	4.590	−1.926	12.7	9.9	11.8	11.4	−5.84

(1) Air wavelength (in Å). (2) Lower excitation potential (in eV). (3) Logarithm of g (lower statistical weight) times f (oscillator strength) (in dex).(4) Equivalent width (in mÅ) at the disk center measured by Grevesse and Sauval (1999). (5) Equivalent width at the disk center (point 00: $\mu = 1$) taken from Table 3 in TU19. (6) Equivalent width at the limb (point 31: $\mu = 0.25$) taken from Table 3 in TU19. (7) Equivalent width for the disk-integrated Sun measured on Kurucz *et al.*'s (1984) solar flux spectrum in the similar manner to that adopted by TU19. (8) Temperature sensitivity parameter calculated at the disk center ($K_{00} \equiv {\rm d}\log W_{00}/{\rm d}\log T$; taken from Table 3 in TU19). The data in Columns (1)–(3) were adopted from Table 1 of Grevesse and Sauval (1999).

Table 3. Resulting center–limb variation of microturbulence.

No.	$\cos\theta$	$\sin\theta$	$\langle\log\epsilon\rangle_0$	σ_0	ξ_0	$\delta\xi$	$\xi_{\rm n}$
(1)	(2)	(3)	(4)	(5)	(6)	(7)	(8)
00	1.0000	0.0000	7.401	0.064	1.13	0.19	1.00
01	0.9995	0.0313	7.409	0.067	1.10	0.20	0.97
02	0.9980	0.0625	7.399	0.071	1.08	0.21	0.96
03	0.9956	0.0938	7.401	0.065	1.10	0.19	0.97
04	0.9922	0.1250	7.408	0.069	1.13	0.20	1.00
05	0.9877	0.1562	7.409	0.068	1.15	0.20	1.02
06	0.9823	0.1875	7.415	0.069	1.12	0.20	0.99
07	0.9758	0.2188	7.413	0.069	1.14	0.21	1.01
08	0.9682	0.2500	7.416	0.067	1.12	0.19	0.99
09	0.9596	0.2812	7.414	0.068	1.13	0.20	1.00
10	0.9499	0.3125	7.414	0.068	1.12	0.20	0.99
11	0.9391	0.3438	7.417	0.070	1.12	0.21	0.99
12	0.9270	0.3750	7.413	0.070	1.15	0.20	1.02
13	0.9138	0.4062	7.413	0.070	1.17	0.21	1.04
14	0.8992	0.4375	7.413	0.069	1.15	0.20	1.02
15	0.8833	0.4688	7.414	0.072	1.16	0.21	1.03
16	0.8660	0.5000	7.414	0.072	1.18	0.21	1.04
17	0.8472	0.5312	7.416	0.070	1.18	0.20	1.04
18	0.8268	0.5625	7.417	0.071	1.20	0.19	1.06
19	0.8046	0.5938	7.416	0.073	1.21	0.21	1.07
20	0.7806	0.6250	7.415	0.072	1.23	0.20	1.09
21	0.7545	0.6562	7.409	0.073	1.27	0.20	1.12
22	0.7262	0.6875	7.410	0.073	1.29	0.20	1.14
23	0.6953	0.7188	7.410	0.074	1.31	0.20	1.16
24	0.6614	0.7500	7.411	0.073	1.34	0.20	1.19
25	0.6242	0.7812	7.412	0.076	1.38	0.21	1.22
26	0.5830	0.8125	7.415	0.073	1.41	0.20	1.25
27	0.5367	0.8438	7.411	0.079	1.50	0.22	1.33
28	0.4841	0.8750	7.408	0.078	1.56	0.20	1.38
29	0.4227	0.9062	7.403	0.078	1.71	0.22	1.51
30	0.3480	0.9375	7.407	0.079	1.89	0.23	1.67
31	0.2480	0.9688	7.421	0.079	2.10	0.24	1.86
Analysis of $W_{\rm d.c.}^{\rm GS}$			7.513	0.053	1.08	0.14	
Analysis of $W_{\rm flux}$			7.434	0.066	1.15	0.17	

(1) Designated number of each observed point (*cf.* Table 1 in TU19). (2) Value of $\cos\theta$ (direction cosine also denoted as μ), where θ is the angle between the line of sight and the normal to the surface. (3) Value of $\sin\theta$, which is equivalent to the concentric radius in unit of the disk radius. (4) Mean of $\log\epsilon$ (logarithmic number abundance of Fe relative to H in the usual normalization of $\log\epsilon_{\rm H} = 12$) at σ_0. (5) Standard deviation (in dex) at the minimum abundance dispersion. (6) Microturbulence solution (in km s^{-1}) defined by the requirement of minimum abundance dispersion. (7) Probable error in ξ (*cf.* Section 3.2). (8) Adjusted microturbulence normalized as $\xi_{\rm n} \equiv \xi_0/1.13$, so that $\xi_{\rm n} = 1$ km s^{-1} may hold at the disk center. In the last two rows are also shown the related results for comparison, which were obtained based on $W_{\rm d.c.}^{\rm GS}$ (disk-center equivalent widths by Grevesse, and Sauval, 1999) and those obtained from $W_{\rm flux}$ (equivalent widths for the disk-integrated Sun).

Table 4. Conditions and results for Fe I 6252.554 flux profile simulations.

No.	$\log\epsilon$	ξ	ζ	$v_{\rm e}$	$W_{\rm cal,flux}$	q_1	Figures
(1)	(2)	(3)	(4)	(5)	(6)	(7)	(8)
0a	7.70	0.5	—	—	123.3	0.170	Fig. 7a,b (solid, pink)
0b	7.56	1.0	—	—	123.7	0.150	Fig. 7a,b (solid, grey)
0c	7.33	1.5	—	—	123.9	0.133	Fig. 7a,b (solid, light green)
1	7.47	$\xi(\theta)$	—	—	123.8	0.143	Fig. 7a,b,c,d (dashed, blue)
2	7.47	$\xi(\theta)$	$\zeta(\theta)$	—	123.8	0.145	Fig. 7c,d (dash-dotted, green)
3	7.47	$\xi(\theta)$	$\zeta(\theta)$	1.9	123.8	0.148	Fig. 7c,d (solid, red)

(1) Case number. (2) Assigned Fe abundance, which was adjusted in advance so that the resulting equivalent width ($W_{\rm cal,flux}$) is almost equal to the observed value ($\approx$ 124 mÅ). (3) Microturbulence, where constant values (in km s^{-1}) were assigned in Cases 0a–c, while θ-dependent microturbulence as described in Equation (1) was assumed in Cases 1–3. (4) Macroturbulence (included only for Cases 2 and 3), for which the θ-dependent anisotropic Gaussian form described by $\zeta(\theta) = 1.5 + 1.0\sin\theta$ (*cf.* Equation (10) in Takeda, 2019) was used. (5) Equatorial velocity of solar rotation, which was included only in Case 3 on the assumption of rigid rotation and equator-on view (inclination angle of $i = 90°$). (6) Equivalent width of the resulting flux profile (in mÅ). (7) First zero frequency in the Fourier transform of the profile (in km^{-1}s) (8) Figure panels where the Fourier transform amplitudes of the relevant profiles are illustrated.

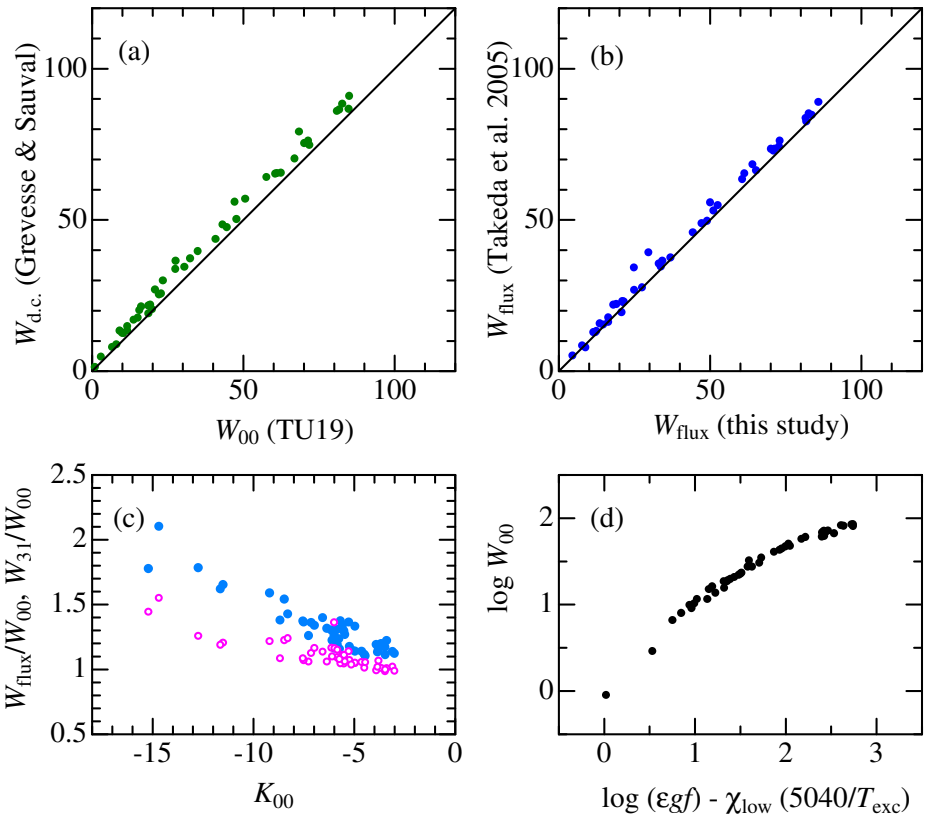

Figure 1. (a) Comparison of Grevesse and Sauval's (1999) disk-center equivalent widths ($W_{\rm d.c.}^{\rm GS}$) for the Fe I lines with those of TU19 (W_{00}) adopted in this study. (b) Comparison of Takeda *et al.*'s (2005) solar flux equivalent widths of Fe I lines (measured by using the direct Gaussian fitting) with those newly evaluated in this study (by following the similar way to TU19). (c) Limb-to-center equivalent width ratios (W_{31}/W_{00}; filled symbols) and flux-to-center ratios ($W_{\rm flux}/W_{00}$; open symbols) plotted against K_{00} (temperature sensitivity parameter). (d) Empirical curve of growth constructed based on the disk-center equivalent widths (W_{00}) of 46 Fe I lines given in Table 2. Here, $\log W_{00}$ data are plotted against $\log\epsilon + \log gf - \chi_{\rm low}(5040/T_{\rm exc})$, where $\log\epsilon$ is the abundance obtained from W_{00} for $\xi = 1$ km s^{-1} and $T_{\rm exc}$ (excitation temperature) is assumed to be 5040 K.

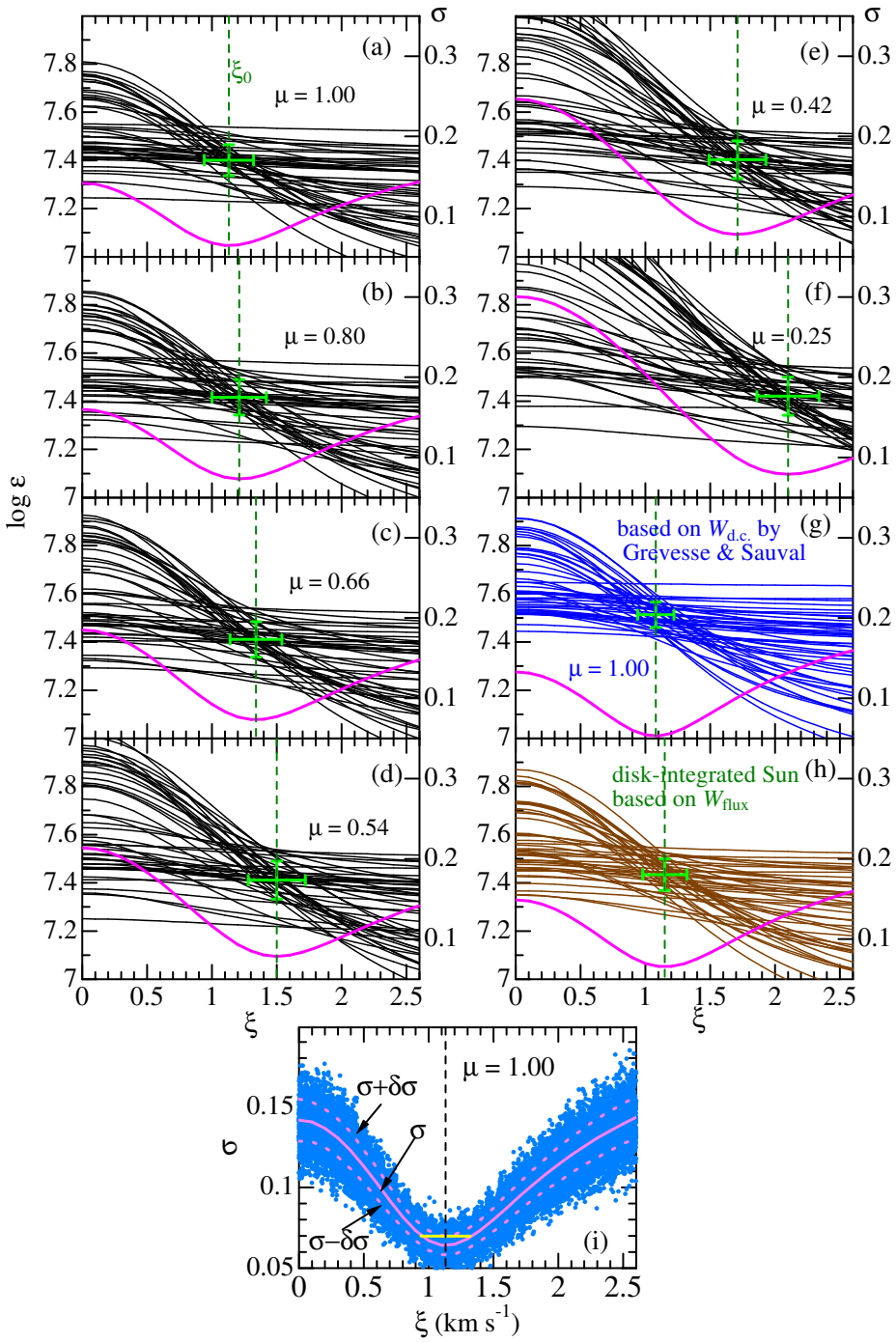

Figure 2. Demonstrative examples of $\log\epsilon$ *vs.* ξ diagrams for selected 8 cases: (a) $\mu = 1.00$, (b) $\mu = 0.80$, (c) $\mu = 0.66$, (d) $\mu = 0.54$, (e) $\mu = 0.42$, (f) $\mu = 0.25$, (g) $\mu = 1.00$ based on Grevesse and Sauval's (1999) $W^{\rm GS}_{\rm d.c.}$ data, and (h) use of $W_{\rm flux}$ for the disk-integrated Sun. In each panel, σ (standard deviation of $\log\epsilon$) is plotted against ξ by the thick (pink) solid line (its scale is marked in the right axis), and the solution of ξ_0 (corresponding to σ_0: σ minimum) is indicated by the vertical dashed line. The green error bars shown at this solution point (ξ_0, $\langle\log\epsilon\rangle_0$) are $\pm\delta\xi$ (probable error in ξ) and $\pm\sigma_0$ (dispersion of $\log\epsilon$). Panel (i) shows the numerical experiment for evaluation of $\delta\xi$, done for the case of $\mu = 1.00$ corresponding to panel (a). Here, randomly generated ($\sigma'_k/\sqrt{2}, k = 1, 2, \ldots, 1000$) at each ξ (*cf.* Section 3.2) are plotted by dots, while their mean (naturally equal to the original σ) and its standard deviation ($\pm\delta\sigma$) are depicted in solid and dashed lines, respectively. The horizontal yellow bar shows the resulting extent of $\pm\delta\xi$ (see the explanation in Section 3.2 for more details).

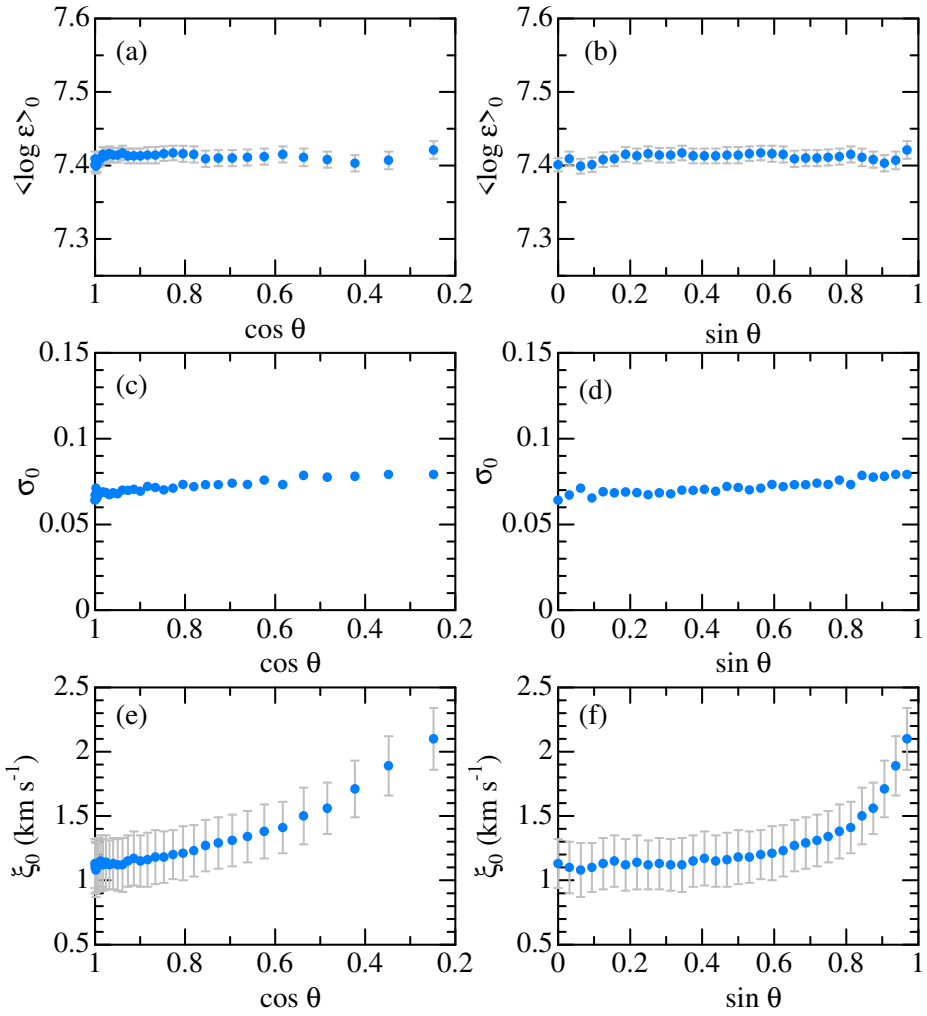

Figure 3. Center–limb variations of $\langle \log \epsilon \rangle_0$ (top), σ_0 (middle), and ξ_0 (bottom), which were determined from the $\log \epsilon$ *vs.* ξ diagrams at each of the 33 points on the solar disk, The results are plotted against $\cos\theta (\equiv \mu)$ and $\sin\theta$ in the left- and right-hand panels, respectively. The error bars attached to $\langle \log \epsilon \rangle_0$ (top panels) denote mean errors ($\pm\sigma_0/\sqrt{N}$, where $N = 46$), while those to ξ_0 (bottom panels) are $\pm\delta\xi$ (probable errors).

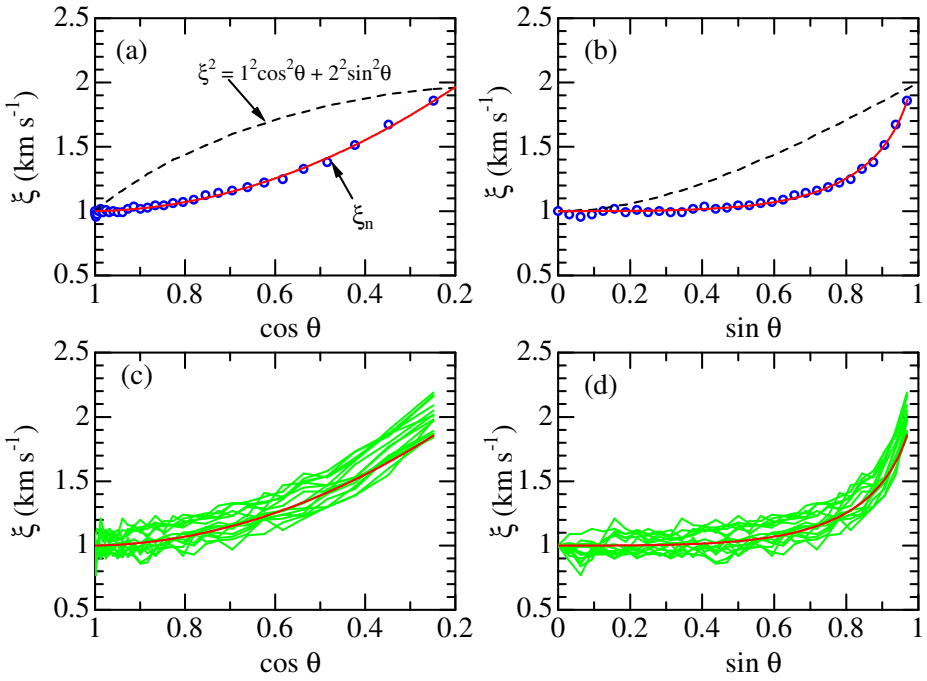

Figure 4. Upper panels: Open symbols illustrate the adjusted angle-dependent solar microturbulence (ξ_n: so normalized as to be 1 km s^{-1} at the disk center), and the best-fit curve (expressed by a quadratic formula: *cf.* Equation (1)) is drawn by the solid line. The expected relation for the case of anisotropic Gaussian distribution (*cf.* Section 4.5) is also shown by the dashed line for comparison. Lower panels: $\xi(\theta)$ relations for each of the 15 lines of medium-to-large strengths ($W_{00} \geq 50$ mÅ) are overplotted by green lines, which were obtained by the requirement of $\log \epsilon(\theta) = \log \epsilon_1$, where $\log \epsilon_1$ is the abundance at the disk center derived from W_{00} by assuming $\xi = 1$ km s^{-1} and $\log \epsilon(\theta)$ is the abundance corresponding to $W(\theta)$ (at the off-center point of angle θ). As in the upper panels, the red line is the best-fit curve of ξ_n.

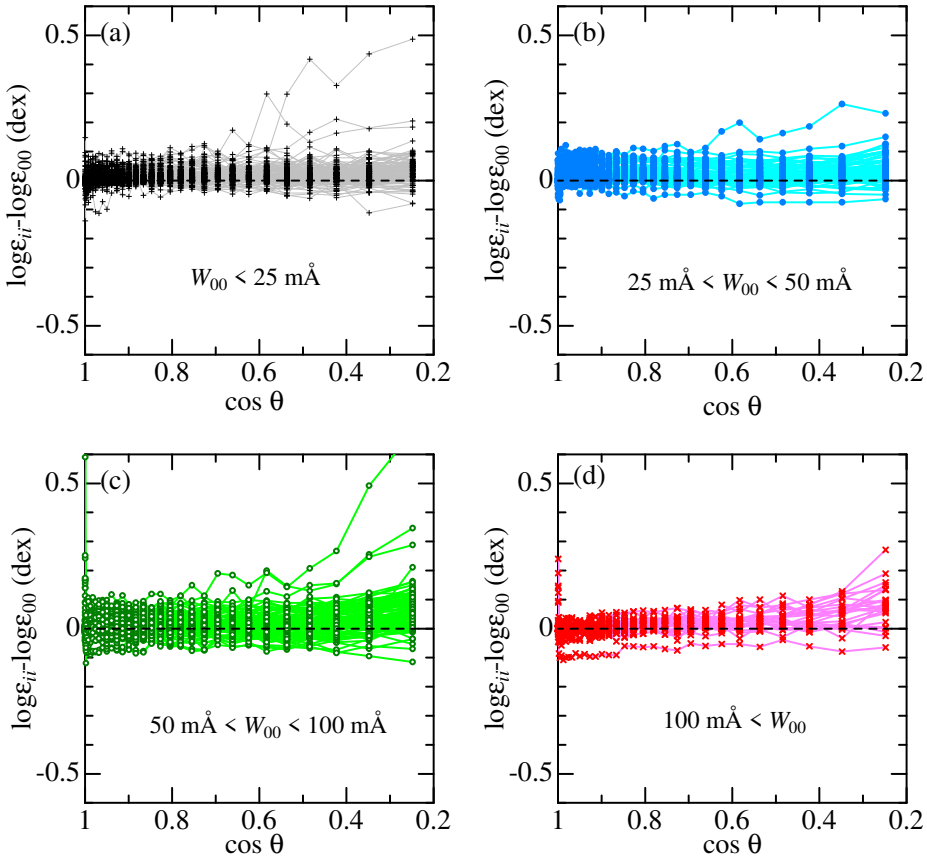

Figure 5. Differences of abundances relative to the disk-center value ($\log \epsilon - \log \epsilon_{00}$) plotted against $\cos\theta$, which were derived based on the solar center–limb equivalent widths (W) of 280 Fe I lines published in TU19 by assuming a μ-dependent microturbulence of Equation (1). Each of the panels (a), (b), (c), and (d) correspond to four line-strength classes, which were grouped according to the disk-center equivalent width (W_{00}): (a) $\cdots$ W_{00} < 25 mÅ (black symbols), (b) $\cdots$ 25 mÅ $\leq W_{00}$ < 50 mÅ (blue symbols), (c) $\cdots$ 50 mÅ $\leq W_{00}$ < 100 mÅ (green symbols), and (d) $\cdots$ 100 mÅ $\leq W_{00}$ (red symbols). These figures should be compared to Figures 10a–d of Takeda (2019), which show the results derived by assuming a constant ξ of 1 km s^{-1}.

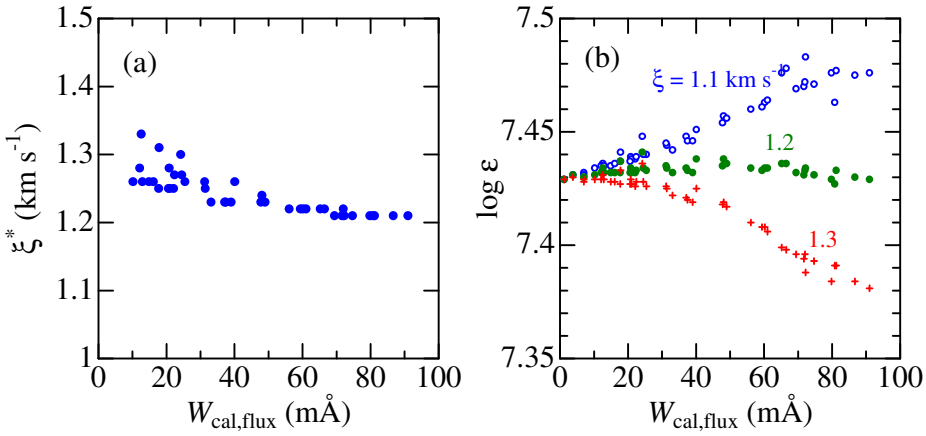

Figure 6. (a) ξ^* *vs.* $W_{\rm cal,flux}$ diagram for the 42 lines satisfying $W_{\rm cal,flux} \geq 10$ mÅ. Here, $W_{\rm cal,flux}$ is the flux equivalent width simulated by the disk-integration method while assuming $\log\epsilon = 7.43$ and $\xi(\theta)$ (Equation (1)), and ξ^* is the value of microturbulence necessary to reproduce $\log\epsilon = 7.43$ if $W_{\rm cal,flux}$ is analyzed in the conventional manner using a constant (*i.e.*, position-independent) ξ. (b) $\log\epsilon$ *vs.* $W_{\rm cal,flux}$ diagram for all the 46 lines, where $\log\epsilon$ is the abundance derived by analyzing $W_{\rm cal,flux}$in the conventional way by using three xi values of 1.1 (open symbols), 1.2 (filled symbols), and 1.3 km s^{-1} (crosses).

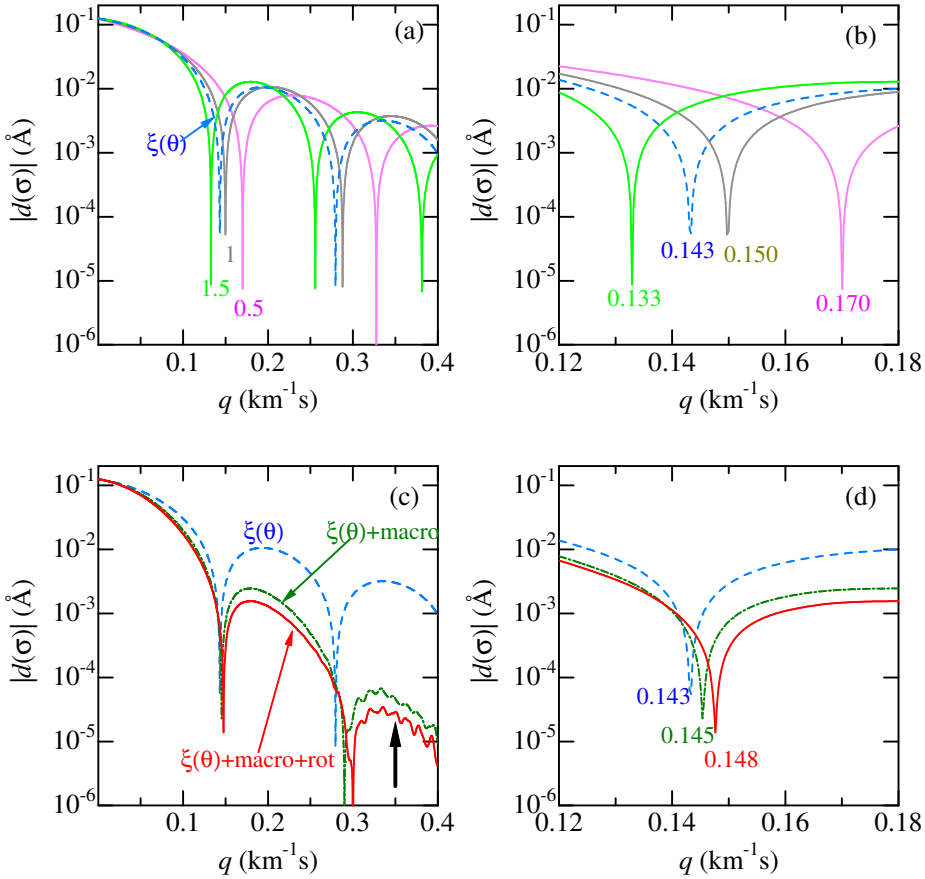

Figure 7. Fourier transform amplitude of the flux profiles of the Fe I 6252.554 line simulated for several test calculations (carried out according to the conditions summarized in Table 4), plotted against wavelength-independent Fourier frequency ($q \equiv \sigma\lambda/c$ in unit of km^{-1}s, where σ is the usual Fourier frequency, λ is the wavelength, and c is the velocity of light). In the upper panels (a, b), the results for Cases 0a–c (cases for three constant microturbulences of 0.5, 1.0, and 1.5 km s^{-1}) and that for Case 1 (θ-dependent ξ) are shown in solid and dashed lines, respectively. The lower panels (c, d) present the results for the three Cases (1, 2, and 3) in order to illustrate the combined effects of (θ-dependent) microturbulence, macroturbulence, and rotation. See the caption of Table 4 for more details. The thick upward arrow in panel (c) indicates the position of the first zero (0.35 km^{-1}s) corresponding to the classical rotational broadening function (for $v_e \sin i = 1.9$ km s^{-1} and the limb-darkening coefficient of $\epsilon \approx 0.6$–0.7). The right-hand panels (b, d) are essentially the same as the corresponding left-hand panels (a, c), except that the region of Fourier frequencies around the first zeros (their values are indicated) is expanded for clarity.